Title
Experimental study on airflow containment and pollutant capture of a push-pull ventilation system in residential kitchens

Journal
Building and Environment, 299

ISSN
0360-1323

Authors
Chen, Wenhua
Yan, Mengyang
Cui, Yunxiang
et al.

Publication Date
2026-07-01

DOI
10.1016/j.buildenv.2026.114676

Building and Environment 299 (2026) 114676

Contents lists available at ScienceDirect

Building and Environment

journal homepage: www.elsevier.com/locate/buildenv

Experimental study on airflow containment and pollutant capture of a push-pull ventilation system in residential kitchens

Wenhua Chen [a], Mengyang Yan [a], Yunxiang Cui [a], Yanzhe Yu [a], Jing Xu [b,*], Junjie Liu [b], Jiayu Li [c]

[a] School of Infrastructure Engineering, Nanchang University, Nanchang, China
[b] Tianjin Key Laboratory of Indoor Air Environmental Quality Control, School of Environmental Science and Engineering, Tianjin University, Tianjin, China
[c] Center for the Built Environment, University of California, Berkeley, CA, USA

ARTICLE INFO

Keywords:
Airflow containment
Capture efficiency
Capture jet
Kitchen ventilation
Particle image velocimetry

ABSTRACT

Cooking is a major source of indoor air pollution, making high-efficiency ventilation systems essential for containing cooking pollutants. This study proposes a novel push-pull ventilation system with an inclined capture jet at the side edge of the stove. Particle image velocimetry and the scattering grayscale method were used to measure airflow characteristics and particle concentration distributions in the cooking zone under different exhaust flowrates, capture jet velocities, and simulated cooking operation disturbances. The results show that the capture jet gradually dominates the cooking zone airflow with increasing velocity, and its centerline aligns with the exhaust outlet, forming a stable containment zone. The deflection angle of the capture jet under heating conditions is larger than that under isothermal conditions. The deflection angle increases with the exhaust flowrate and decreases with the jet velocity. Empirical linear models for jet centerline trajectory and velocity decay can accurately describe these relationships. Cooking operation disturbances increase the thermal plume radius and the capture jet entrainment radius but have negligible impacts on the jet deflection angle at 0.8 m/s. The capture jet effectively reduces high-turbulence zones and enhances pollutant containment. Cooking operation disturbances reduce total particle capture efficiency (CE) by up to 5%, and this reduction increases with disturbance speed. The ventilation system exhibits optimal containment and capture performance at a jet velocity of 0.8 m/s, achieving total CEs of 95.9%–97.1% at exhaust flow rates of 360–480 m^3/h. Compared to corresponding cases without the capture jet, the new system improves total CE by up to 14%.

1. Introduction

Cooking constitutes a fundamental daily routine across households worldwide while also serving as the principal contributor to indoor air pollution within dwellings [1,2]. The cooking process generates significant quantities of pollutants within brief time intervals [1,2], including gaseous pollutants, particulate matter (PM), and other harmful substances [3,4]. Extended exposure to such pollutants elevates the likelihood of lung cancer, and respiratory ailments [5]. High-performance exhaust systems are therefore imperative to contain cooking pollutants and prevent their spread into living spaces.

Past studies have proposed many measures to enhance range hood capture efficiency (CE), such as modifying the design of the range hood, adding plates and capture jets [6–8]. Range hoods incorporate the capture jet can prevent spillage of cooking pollutants from the hood at a low exhaust rate [9]. The air curtain formed by the capture jet can also effectively improve the CE of the range hood. In the relevant literature, two main types of capture jets can be identified: downward and upward capture jets [7,9]. The downward capture jets are usually installed with one or three slots along the lower edge of the exhaust hood [10,11]. The downward capture jets can prevent the spillage of cooking pollutants from the hood and reduce individual exposure levels [10,11]. The individual exposure level of cases with downward capture jets can be reduced to 10^{-5}–10^{-6} of the baseline case without the capture jets [10,11]. The optimal air velocity of downward capture jets with one and three slots is around 1.8–2.5 m/s [11] and 1.5 m/s [10], respectively. However, downward capture jets may collide with the fluctuating cooking thermal plumes due to the complex turbulence characteristics [12], thus leading to the leakage of cooking pollutants [11].

Furthermore, previous investigations have explored three types of

* Corresponding author.
E-mail address: xu_jing@tju.edu.cn (J. Xu).

https://doi.org/10.1016/j.buildenv.2026.114676
Received 2 March 2026; Received in revised form 23 April 2026; Accepted 27 April 2026
Available online 28 April 2026

upward capture jets around the stove: one [13], three [11,14,15], and four slots [16,17]. The upward capture jets not only enhance the CE of the exhaust hood [16,18] but can also significantly reduce the individual exposure levels [11,13,19]. Some studies investigated the effect of the upward capture jets with 4 slots on the pollution control in a Chinese kitchen [16] and a kitchen island [17]. For cases with four-slot upward capture jets, the CO_2 concentration around the breathing zone was reduced to 0.4–0.5 times that of the baseline case without capture jets [16,17]. Furthermore, the CO_2 CE for cases with 4 slots upward capture jets increased by 7.5% compared to the base case [16]. The upward capture jets with 3 slots around the burner can create a clean area directly in front of the human body [11]. However, this clean area is sensitive to the air speed of capture jets [11]. By comparison, the upward capture jets with 3 slots around the stove have been explored in many studies [14,15,18,19]. Compared with the baseline case, the CE of a downdraft [15] and an updraft range hood [18] combined with 3 slots jets around the stove increased by 14.5% and 9.7%, respectively. In the above studies [11,15,18,19], the upward capture jets all with an angle of 90°. A higher jet velocity may collide with the lower edge of the exhaust hood, causing pollutant spillage through entrainment, especially under lower exhaust flowrates. The majority of flowrates measured in range hoods were only 258–534 m^3/h in Chinese residential buildings [20]. Furthermore, there is also controversy regarding the impact of the fully enclosed air curtain (3 and 4 slots) on the combustion efficiency of the gas stove. Huang et al. [13] found that an upward capture jets of one slot at the front edge of the stove resist the adverse impact of cross-draft and increase the CE of the ventilation system. The mannequin with the cooking operation in front of the stove may disrupt the stability of the capture jet, thereby causing the leakage of cooking pollutants [21]. Moreover, no conclusion was given as to which form of captured jet was more effective in the aforementioned studies.

Apart from the cross draft [13], cooking behavior can also cause air disturbance, thereby reducing the CE of the exhaust hood. The impacts of human standing and walk-by motions have been emphasized in previous investigations. Huang et al. [19] found that the CE of the exhaust hood in unoccupied cases was 0.1%−2.4% larger than that in occupied cases. Some studies [22,23] investigated the effects of disturbance by long-term human walk-by motions on the CE of the ventilation system in commercial kitchens. Iwamatsu et al. [23] found that the CE of the hood reduced with increasing human movement frequency. Long-term human walk-by disturbances could reduce the CE by up to 20%. Lv et al. [24,25] focused on the impact of short-term human walk-by disturbances on the transient CE of the exhaust hood. The transient CE could be reduced by up to 0.5 [24,25]. Compared to human walk-by disturbances, the cooking operation above the pan is much more complicated and cannot be ignored. However, the impact of the cooking operation disturbance on the CE of the exhaust hood is rarely analyzed in previous studies.

To address the containment challenges identified in previous designs, such as jet-hood collision and sensitivity to disturbances, this study proposes a novel push-pull exhaust system featuring an upward capture jet located at the side edge of the stove with an inclined angle. This configuration aims to create a more stable and effective airflow containment zone that integrates seamlessly with the exhaust flow, thereby minimizing pollutant spillage.

Thus, this investigation aims to determine the flow characteristics and pollutant containment performance of a new push-pull exhaust system in residential kitchens. Particle image velocimetry (PIV) [26] and the scattering grayscale method [27–29] were used to measure airflow characteristics and particle concentration distributions in the cooking zone under different exhaust flowrates, capture jet velocities, and simulated cooking operation disturbances. The air velocity, turbulence intensity (Tu), vorticity, and particle concentration (grayscale) fields were investigated based on the measured data. The deflection trajectory and centerline velocity decay of the capture jet were quantified and compared across different conditions, after which corresponding empirical linear models were established. The effects of the capture jet and simulated cooking operation disturbances on the capture performance of the new exhaust hood were evaluated using CE and particle concentration measurements in the cooking zone.

2. Methods

2.1. Experimental mockup

As shown in Fig. 1, experiments were conducted in a kitchen cabin. The cabin has dimensions of 2.7 m (X) × 2.0 m (Y) × 2.3 m (Z). The cabin was placed in a large thermostatic chamber maintained at 22±0.5 °C. A nonstick pan (diameter 240 mm) was placed on an electric stove with an equivalent heating area. The pan center was positioned 0.22 m from the wall. The distance between the center of the pan and the center of the exhaust outlet was 200 mm. The pan was heated to a temperature of 260±1 °C under heating conditions, according to the IEC (2011) [30] and GB/T 17713 (2011) [31]. The dimensions of the inlet are 390 mm × 240 mm. The distances from the center of the air inlet to the wall were 1350 mm and 320 mm in the x- and y-directions, respectively. The exhaust outlet of the range hood measured 400 mm in long and 200 mm in wide. The distances from the center of the exhaust outlet to the wall were 1350 mm and 220 mm in the x- and y-directions, respectively. The distance between the cooking table and the exhaust hood was 750 mm.

Fig. 2a presents the principle diagram of the capture jet. Fig. 2b shows the diffuser of the capture jet containing 19 linear slots. The dimensions of the capture jet diffuser are 50 mm × 300 mm. The dimensions of each linear slot are 40 mm (h) × 10 mm. The air velocity along the diffuser was approximately uniform. The supply angle is 47.5°. A motor-driven aluminium plate (Fig. 2c) rotating clockwise was used to simulate the interference caused by cooking operations above the pan. The sketch-up of the disturbance generator is presented in Fig. 2c. To discuss the impact of cooking operations on pollutant capture efficiency, the rotational speed of the disturbance generator was set at two values (30 and 60 rpm).

2.2. PIV setup

The airflow and particle concentration (grayscale) distributions in the cooking zone were measured using PIV [26] and a scattering grayscale method under different exhaust flowrates, capture jet velocities, and simulated cooking operation disturbances. The particle images were also acquired employing the PIV system. Table 1 lists the measurement setup of the PIV system. The measurement section of the air velocity field and particle concentration (grayscale) field is shown in Fig. 1. Two measurement sections overlap. To achieve a time-independent velocity field, 540 instantaneous velocity fields were continuously sampled over

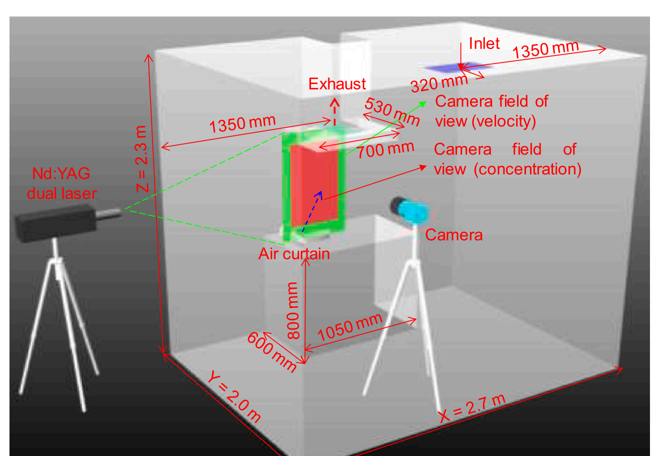

Fig. 1. Schematic diagram of experimental mockup.

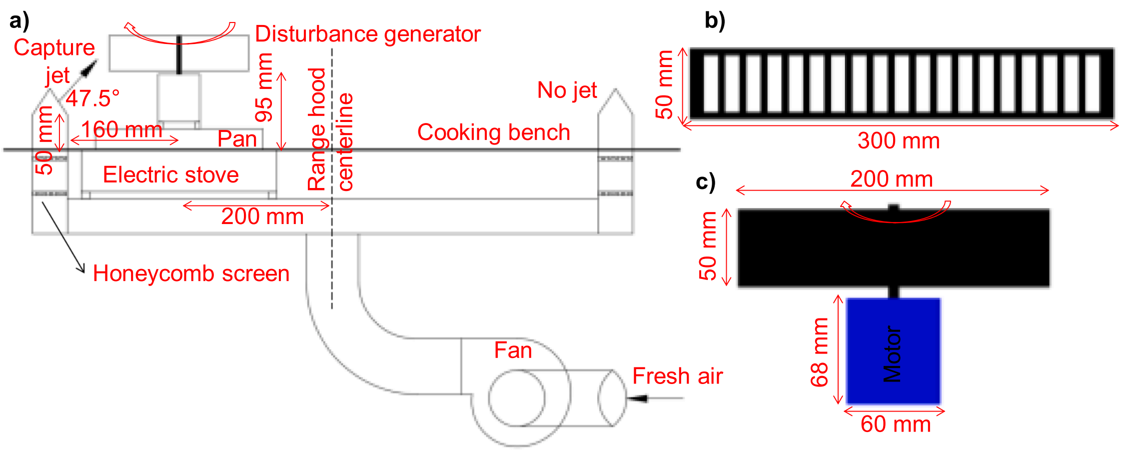

Fig. 2. (a) Principle diagram of the capture jet; (b) Dimensions of the capture jet diffuser; (c) Sketch of the disturbance generator.

Table 1
PIV measurement setup.

Laser source	Neodymium-doped Yttrium Aluminum Garnet (Nd: YAG) dual-pulse laser
Laser power	350 mJ/pulse
Charge coupled device (CCD) model	FlowSense EO 11M
Lens	Nikon Nikkor 50 mm Lens
Visual field of CCD	4032 pixels × 2688 pixels
Size of interrogation window	48 pixels × 48 pixels
Sampling frequency	3 Hz
Tracing particles	Diisooctyl sebacate (DEHS)
Sampling frequency	≈ 1 µm
Diameter of trace particles	1 mm
Velocity field of view	966 mm × 645 mm
Concentration field of view	645 mm × 484 mm

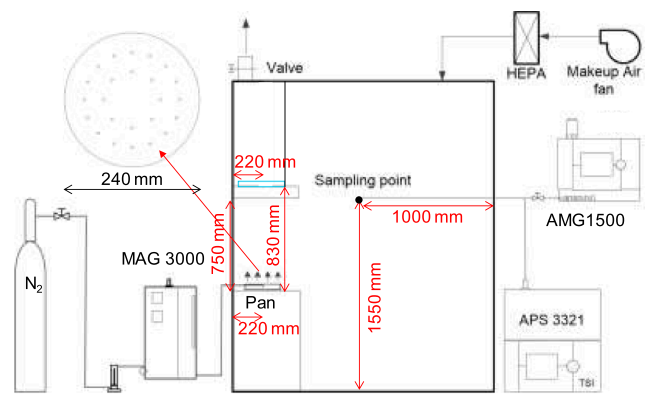

Fig. 3. Experimental configuration of kitchen and particle sampling method.

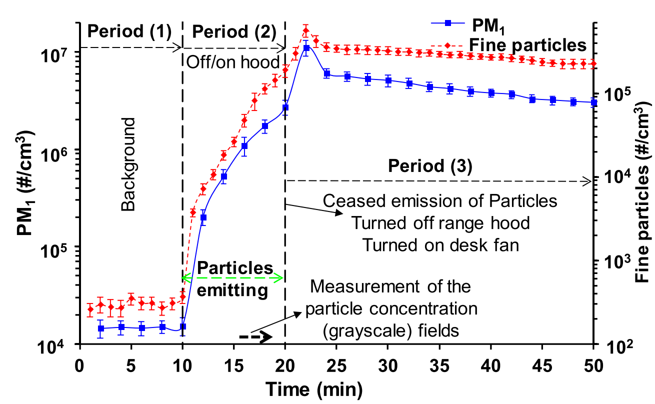

Fig. 4. Test procedure for particle capture efficiency and measured particle concentration with the range hood off during period (2). Error bars represent standard deviation.

3 min. The trace particles were generated by a smog generator (PIV-part40, PIVTEC GmbH) and were evenly distributed in the kitchen cabin during velocity field measurements. The "Dynamic Studio" software was used to analyze the particle images. The first step involved removing background noise from the raw images via background subtraction. Subsequently, the velocity vectors were calculated by the multi-grid adaptive correlation method incorporating high-precision sub-pixel interpolation.

For 2-dimensional PIV systems, the total systematic error contributed by other factors is 1–2% [32]. The convergence of the time-averaged velocity was analyzed using the central limit theorem [33] to evaluate the main statistical error. Eq. (1) was applied to determine the statistical error V_r of time-averaged velocity [33].

$$V_r = \frac{1}{\sqrt{N}} \frac{z_\alpha}{2} \frac{v_{RMS}}{V} \tag{1}$$

where N is sampling number (540). V is the local time-averaged velocity. v_{RMS} is the root mean square of the local velocity. z_α /2 is a variable related to the confidence level. The statistical error of PIV in the cooking zone was quantified at the range of 3.4–7.3% in this study.

Trace particles for measurement the particle concentration fields were generated by a particle generator (MAG 3000, PALAS) and emitted from the pot (Fig. 3). The continuous sampling of instantaneous particle concentration fields was also acquired for 540 films within 3 min (16th-18th in Fig. 4). For some cases, the velocity field was also measured under isothermal conditions to clarify the impact of the cooking plumes on the capture jet. Under isothermal conditions, the pan was not heated. The measurement conditions are summarized in Table 2.

2.3. Calculation of CE

As shown in Fig. 3, the trace particles generated by the MAG 3000 were used to simulate the cooking particles. The physical properties of DEHS are similar to those of edible oils, with a density of 912 kg/m^3 and a low evaporation rate [34]. The emission method of trace particles was based on the Ref. [35]. The particle emission flowrate was 3.5 L/min, controlled by a gas rotameter. The particle number concentrations were monitored by applying a condensation particle counter (CPC) (AMG 1500, MSP) and an Aerodynamic Particle Size (APS 3321, TSI). The

Table 2
Experimental cases setup.

Case	Exhaust flowrate (Q) (m^3/h)	Capture jet velocity (V_0) (m/s)	Conditions
1	300	0	isothermal (iso)
2	300	0	heating - 0 rpm
3	300	0	heating - 30 rpm
4	300	0	heating - 60 rpm
5	300	0.4	isothermal
6	300	0.4	heating - 0 rpm
7	300	0.4	heating - 30 rpm
8	300	0.4	heating - 60 rpm
9	300	0.8	isothermal
10	300	0.8	heating - 0 rpm
11	300	0.8	heating - 30 rpm
12	300	0.8	heating - 60 rpm
13	300	1.2	isothermal
14	300	1.2	heating - 0 rpm
15	360	0	heating - 0 rpm
16	360	0.4	isothermal
17	360	0.4	heating - 0 rpm
18	360	0.8	isothermal
19	360	0.8	heating - 0 rpm
20	360	0.8	heating - 30 rpm
21	360	0.8	heating - 60 rpm
22	360	1.2	isothermal
23	360	1.2	heating - 0 rpm
24	480	0	heating - 0 rpm
25	480	0.8	isothermal
26	480	0.8	heating - 0 rpm

sampling frequency of the APS 3321 and AGM 1500 was 1 and 2 min, respectively. The APS 3321 and AGM 1500 with a sampling flowrate of 1 and 0.3 L min^{-1}, respectively. The sampling dilution ratio for the APS 3321 and AGM 1500 was 1:100 and 1:25, respectively. The APS 3321 measured fine particles from 0.542–20 μm. The measurement range of the AGM 1500 was set as 35–940 nm with 24 channels. The concentration accuracy of the APS 3321 is ±10% of reading plus variation from counting statistics. The concentration accuracy of the AGM 1500 is ±10% relative to the standard MSP CPC.

Fig. 4 shows the test procedure for particle capture efficiency. The background concentration $C_{background}$ was monitored during period (1). The pan was heated during period (1). Tracer particles were released during period (2). The emission strength of particles was determined with the range hood off in period (2). The residual emission strength of particles was measured with the range hood on in period (2) to determine the capture efficiency of the ventilation system [36]. In period (3), the release of tracer particles was stopped. Simultaneously, the range hood was turned off and the desk fan was turned on. Each test was repeated five times. As shown in Fig. 4, the standard deviation of particle number concentrations in period (3) was small. Therefore, complete mixing was assumed in the kitchen during period (3). The peak concentration C_p and the time t_p can be obtained from the concentration data in period (3).

The particle mass balance equation can be estimated using Eq. (2) [37].

$$\frac{dC_{in}}{dt} = P\alpha C_{out} - (\alpha + K)C_{in} + \frac{S}{V} \tag{2}$$

where C_{in} = indoor particle concentration. C_{out} = outdoor particle concentration. P = penetration coefficient of kitchen envelope. α= air exchange rate. K = decay rate of particles. S is the source strength. V is the volume of the kitchen. All cracks were sealed, and the range hood was off during period (3). Thus, only the natural decay rate K was considered in the present study.

In the period (3), the particle mass balance equation can be fitted by Eq. (3) [37,38].

$$C_{in}(t) = C_p e^{-K(t-t_p)}\ t \geq t_p \tag{3}$$

The source strength $S_{hood-off}$ and residue strength $S_{hood-on}$ of particles can be calculated by Eqs. (4) and (5), respectively [37,38].

$$S_{hood-off} = K_{hood-off}\Delta C_{in,hood-off}V / ((1 - e^{-K_{hood-off}t}) \tag{4}$$

$$S_{hood-on} = K_{hood-on}\Delta C_{in,hood-on}V / ((1 - e^{-K_{hood-on}t}) \tag{5}$$

where $\Delta C_{in} = C_{in}(t) - C_{background}$.$S_{hood-on}$ is the residue source strength with the hood on in period (2) (in Fig. 4). $S_{hood-off}$ is the source strength with the hood off in period (2).

The total particles CEs were calculated through an indirect method [39].

$$CE = 1 - S_{hood-on} / S_{hood-off} \tag{6}$$

2.4. Emission characteristics of trace particles for capture performance test

Fig. 4 presents the time-resolved particle concentrations with the range hood off during period (2). Fig. 5 shows the measured number distribution (NP) and calculated volume distribution (MP) of trace particles for the capture performance test. The number distribution of trace particles shows a single-modal distribution. The number mode diameter is 113 nm. This single-modal distribution is in agreement with the PM_1 (particles with diameter < 1 μm) generated by commercial cooking and heating oil [40]. The number mode diameters of different cooking particles ranged from 100–160 nm, including Chinese and Western style cooking [40]. The cumulative frequency of NP indicates that PM_1 accounts for more than 90% of the total number concentration. The calculated volume distribution of trace particles shows a bimodal distribution. These results are consistent with those of cooking particles [41]. The major and minor volume mode diameters are 0.898 and 5.048 μm, respectively. Although the mode diameters differ slightly from those of cooking particles [41], these size distribution characteristics suggest that the trace particles could accurately represent those of cooking particles. The relative standard deviation for the averaged frequency of NP and MP ranged from 4.2% to 18.9%. These values are close to the experimental results of oil heating [34]. The small standard deviation in Fig. 5 demonstrates good repeatability of the tracer particles.

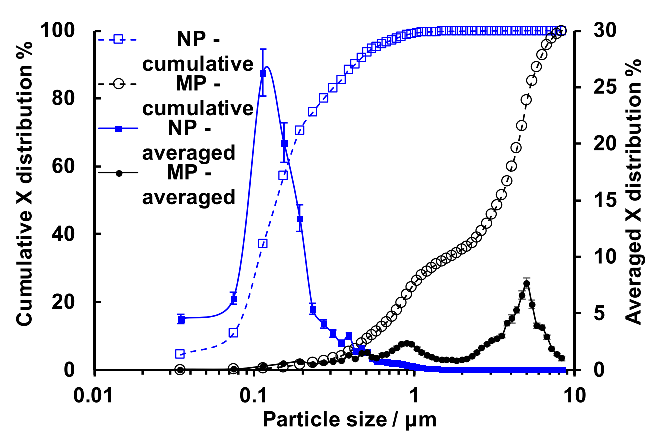

Fig. 5. Measured number distribution (NP) and calculated volume distribution (MP) of trace particles for capture performance test. Error bars represent standard deviation.

3. Results and discussion

3.1. Flow statistics

Fig. 6 compares the velocity fields of selected cases (see Table 2) under isothermal and heating conditions. The velocity vector $V_{xz} = \overrightarrow{V}_x + \overrightarrow{V}_z$, where V_x and V_z are the velocity components in the section. The airflow pattern in Fig. 6a agrees with that of a top suction range hood in our previous study [26]. The flow field in the cooking zone under heating conditions was dominated by the cooking thermal plumes, as shown in Fig. 6a. The thermal plumes deviated to the left side of the pan. It might be due to the plume entrainment imbalance from the confined space. The velocity fields in Fig. 6b–e indicate that the flow field in the cooking zone was dominated by the capture jet driven forced convection under isothermal conditions at lower exhaust flowrates. As for the cases under heating conditions, the flow field in the cooking zone was also gradually dominated by the capture jet with the increase of jet velocity (Fig. 6b–d). The center velocity of thermal plumes in Fig. 6b was significantly higher than that in Fig. 6a. This is likely because the low-velocity capture jet is entrained by the thermal plume, thereby enhancing the intensity of the thermal plumes. As shown in Fig. 6, the deflection angle of the capture jet under heating conditions is larger than the corresponding case under isothermal conditions. It is due to the impact of the cooking thermal plumes. The airflow pattern in the cooking zone was gradually dominated by the suction flow with the increase of exhaust flowrate (see Fig. 6e, f). Meanwhile, the velocity vectors in Fig. 6e, f indicate that the suction flow and capture jet can be well combined to form a cohesive containment system that effectively suppresses the thermal plume and channels the airflow toward the

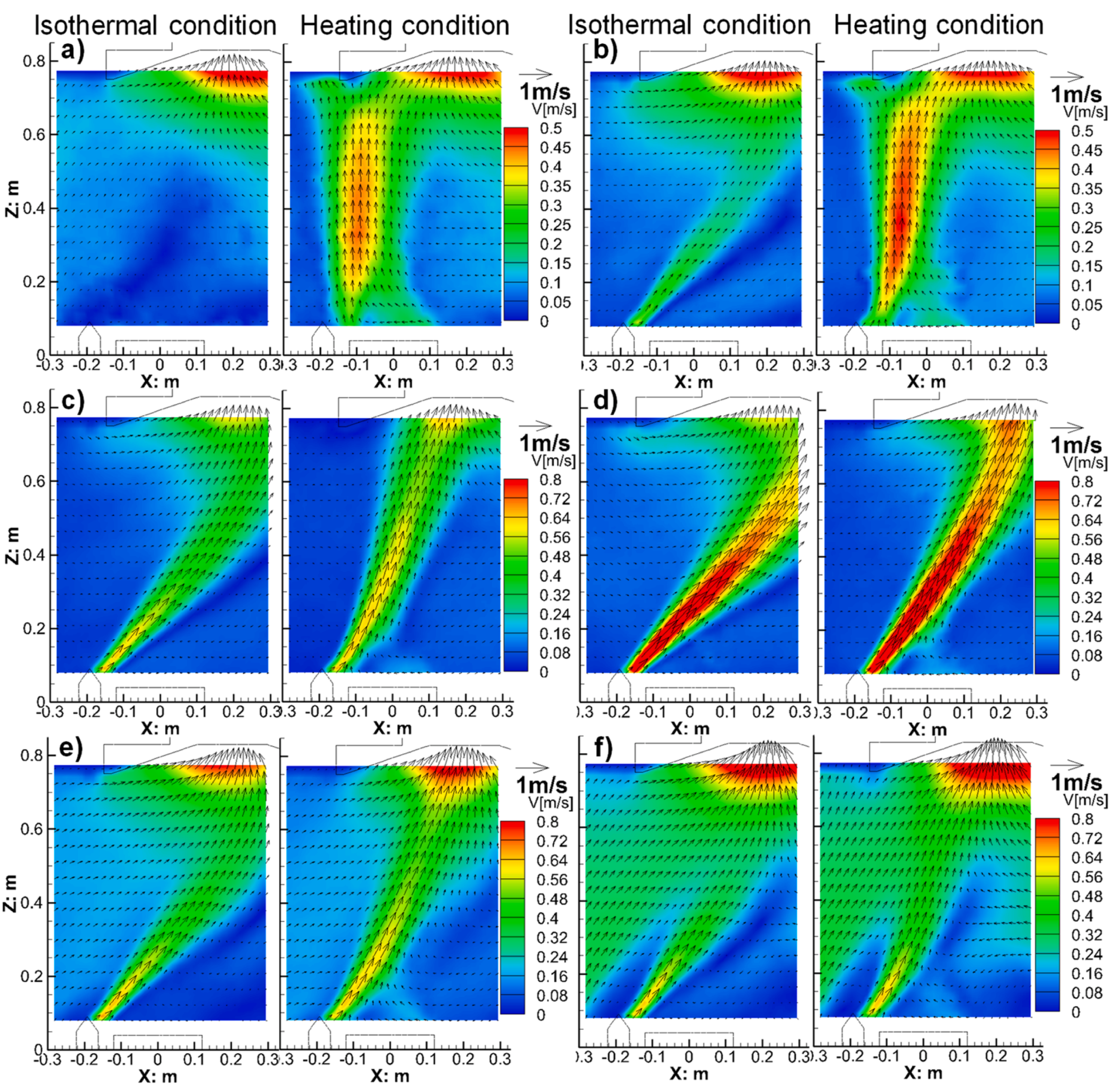

Fig. 6. Time-averaged velocity fields of cases under isothermal/heating condition: (a) 300 m^3/h - 0 m/s; (b) 300 m^3/h - 0.4 m/s; (c) 300 m^3/h - 0.8 m/s; (d) 300 m^3/h - 1.2 m/s; (e) 360 m^3/h - 0.8 m/s; (f) 480 m^3/h - 0.8 m/s.

exhaust.

Fig. 7 presents the velocity fields of cases with the disturbance generator operating at two speeds: 30 rpm and 60 rpm (see Table 2). By comparing the velocity fields in Figs. 6a and 7a, b (or Figs. 6b and 7c, d), it can be observed that the disturbance can increase the radius of the cooking thermal plumes. This is consistent with the thermal plumes generated by a rotating heated plate [42]. The comparison results also show that the center velocity of thermal plumes decreases with increasing disturbance speed. This may be because the disturbance induces a vortex flow in the cross-section, thereby reducing the center velocity. By comparing the velocity fields in Figs. 6c and 7e, f (or Figs. 6e and 7g, h), it can be found that the disturbance can increase the entrainment radius of the capture jet. And the entrainment radius increases with the disturbance speed. Meanwhile, the center velocity of the capture jet decreases with the disturbance speed. Fig. 7e–h indicate that the influence of disturbance on the deflection angle of the capture jet is not significant, compared to the velocity fields of cases without disturbance. This result demonstrates the stability of the airflow containment under typical cooking disturbances at a jet velocity of 0.8 m/s.

The Tu distributions of some cases (in Table 2) were given in Fig. 8. Tu is delineated as $Tu = \sqrt{\langle v'^2 \rangle}/V$, where v' is the fluctuation of instantaneous velocity. Fig. 8a shows that the cooking zone has a high Tu value under isothermal conditions. Due to the low air speeds and large fluctuation in this area. As depicted in Fig. 8b–d, the Tu distributions of cases without a capture jet are controlled by the disturbance of the cooking plume under heating conditions. The high-Tu zone is located on the left side of the pan. By comparing the Tu distributions in Fig. 8b–d, it can be found that the disturbance can increase the area of the high-Tu zone. Moreover, another high-Tu zone is located at the right side of the pan with the disturbance speed at 60 rpm. These zones with low velocity and high-Tu will preserve pollutants. Fig. 8e–h show that the Tu distributions of cases are dominated by the capture jet and slightly affected by the disturbance. The high Tu zone under heating conditions is located at the right side of the capture jet (see Fig. 8f, h). By comparing the Tu distributions in Fig. 8f–h, it can be found that the disturbance can decrease the area of the high-Tu zone. It indicates that the capture jet will help the containment and extraction of pollutants.

3.2. Vorticity field

The vorticity ω is used to further characterize the rotation trend of airflow. The vortex identification method is delineated as follows [12]:

$$\omega = \frac{\partial V_z}{\partial x} - \frac{\partial V_x}{\partial z} \tag{7}$$

$$W = \langle \omega \rangle \tag{8}$$

where W is time-averaged vorticity, s^{-1}. The W distributions of some cases (in Table 2) were displayed in Fig. 9. Fig. 9a depicts that the surface layer of the range hood formed a positive vortex under isothermal conditions due to the viscous effect. Fig. 9b–d compares the W for the cases with different disturbance speeds. The rotational tendency in the region of the thermal plume is stronger. The vorticity structure of cases under heating conditions is controlled by two pairs of vortices in opposite directions, as shown in Fig. 9b–d. The rotational

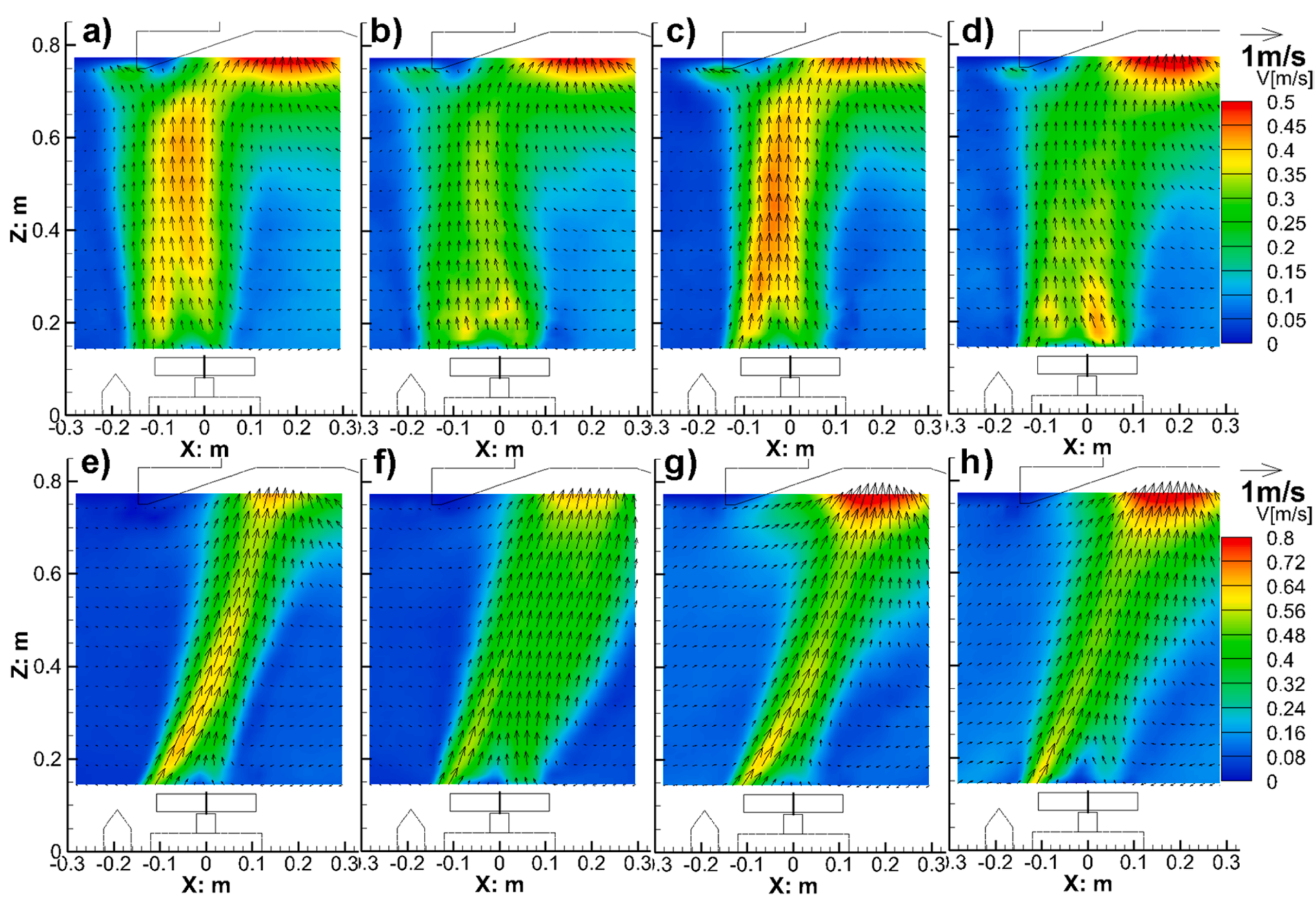

Fig. 7. Time-averaged velocity fields of cases with disturbance under heating condition: (a) 300 m^3/h - 0 m/s - 30 rpm; (b) 300 m^3/h - 0 m/s - 60 rpm; (c) 300 m^3/h - 0.4 m/s - 30 rpm; (d) 300 m^3/h - 0.4 m/s - 60 rpm; (e) 300 m^3/h - 0.8 m/s - 30 rpm; (f) 300 m^3/h - 0.8 m/s - 60 rpm; (g) 360 m^3/h - 0.8 m/s - 30 rpm; (h) 360 m^3/h - 0.8 m/s - 60 rpm.

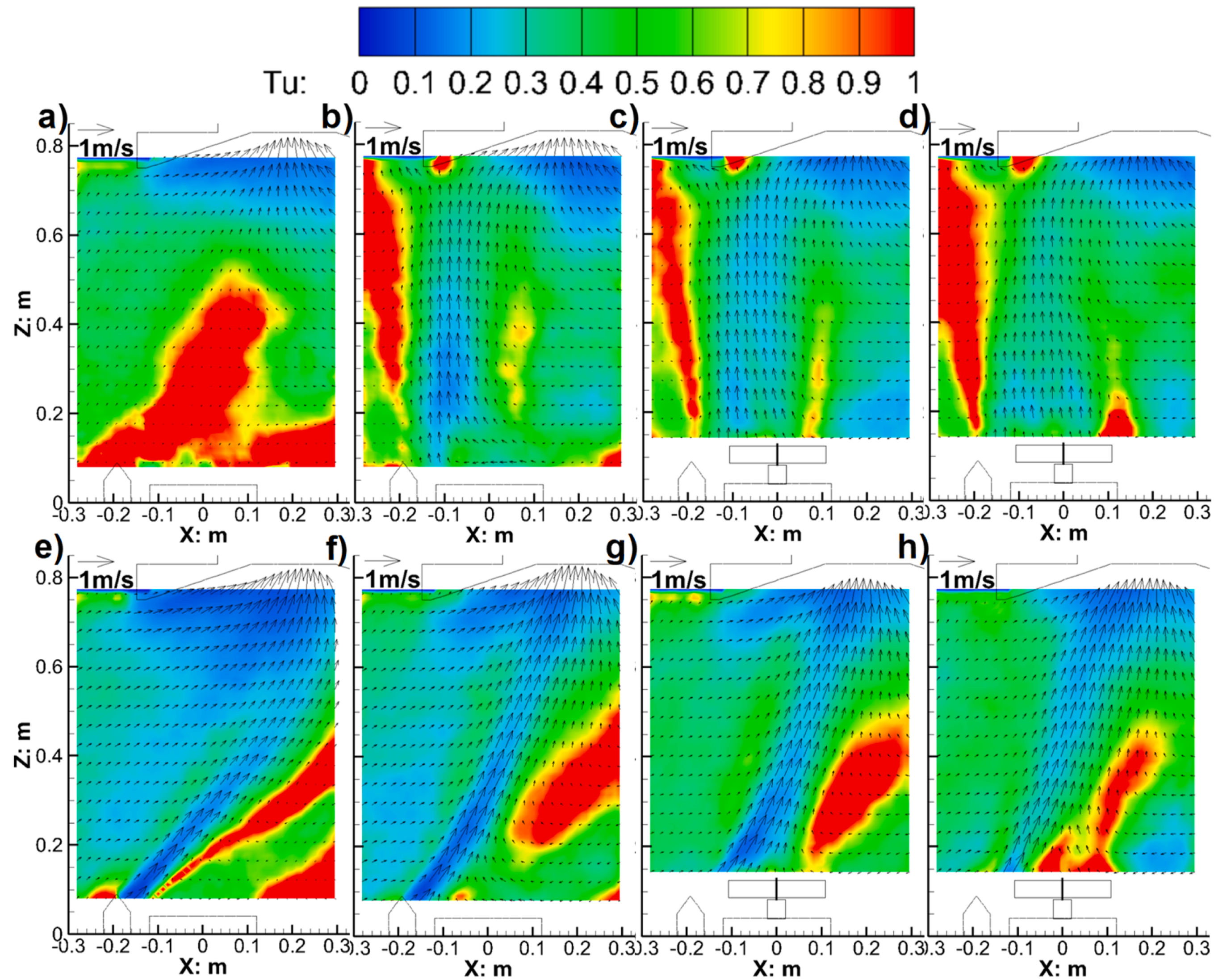

Fig. 8. Tu of fluctuating velocities for cases: (a) 300 m^3/h - 0 m/s - iso; (b) 300 m^3/h - 0 m/s - heating; (c) 300 m^3/h - 0 m/s - 30 rpm; (d) 300 m^3/h - 0 m/s - 60 rpm; (e) 360 m^3/h - 0.8 m/s - iso; (f) 360 m^3/h - 0.8 m/s - heating; (g) 360 m^3/h - 0.8 m/s - 30 rpm; (h) 360 m^3/h - 0.8 m/s - 60 rpm.

tendency on the left side of the pan is stronger than that on the right side. It might be due to the restricted suction on the right side of the thermal plume. Moreover, the vorticity tendency decreases with increasing disturbance speed. It might be because the disturbance causes the thermal plume to exhibit a vortex flow in the cross-section, thereby resulting in a decrease in the V_{xz} and W. Fig. 9e demonstrates that the vorticity structure of the capture jet exhibited symmetry about the jet centerline under isothermal conditions. Fig. 9e–h show that the vorticity structure of cases with a capture jet is dominated by the jet flow. While the vorticity structure of the capture jet exhibited an asymmetric distribution about the jet centerline under heating conditions (see Fig. 9f–h). Fig. 9f shows that the cooking thermal plumes made a significant upward deflection in the W distribution. By comparing the W distributions in Fig. 9f–h, it can be found that the disturbance can decrease the vorticity magnitude on the right side of the capture jet. The reduction in vorticity magnitude on the right side of the jet suggests that disturbance weakens the local rotational flow structures, which, while part of the containment zone, may also indicate a slight loss of coherence in the airflow barrier. However, the vorticity magnitude on the left side was less affected by the disturbance. This result also indicates that the capture jet at 0.8 m/s has a relatively strong anti-disturbance capability.

3.3. *Capture jet flow characteristics*

To further investigate the capture jet flow characteristics, the centerline velocity decay law was analyzed. The dimensionless trajectories of capture jet centerline velocity at different conditions are compared in Fig. 10. The dashed lines in Fig. 10a paint the centerlines of the capture jet under isothermal conditions. The low exhaust flowrate has less effect on the deflection degree of the capture jet at $V_0 = 1.2$ m/s. The centerlines of the capture jet were nearly coincident below Z/h = 12 for the cases with $V_0 = 1.2$ m/s (see Fig. 10a). The solid lines in Fig. 10a paint the centerlines of the capture jet under heating conditions. The deflection degree of the capture jet under heating conditions is larger than that in corresponding cases under isothermal conditions. The thermal plumes have notable impacts on the deflection degree of the capture jet, especially for the cases with low Q and V_0. As shown in Fig. 10a, the deflection degree of the capture jet increases with Q and decreases with V_0, both for isothermal and heating conditions. Fig. 10b compares the trajectories of the capture jet centerline velocity for the cases with and without disturbance. Although the disturbance had a non-negligible impact on the velocity field (see Fig. 7) and vorticity field (see Fig. 9) on the right side of the capture jet, the influence of the disturbance on the deflection angle of the capture jet was negligible. This is attributed to the disturbance has a minor influence on the center

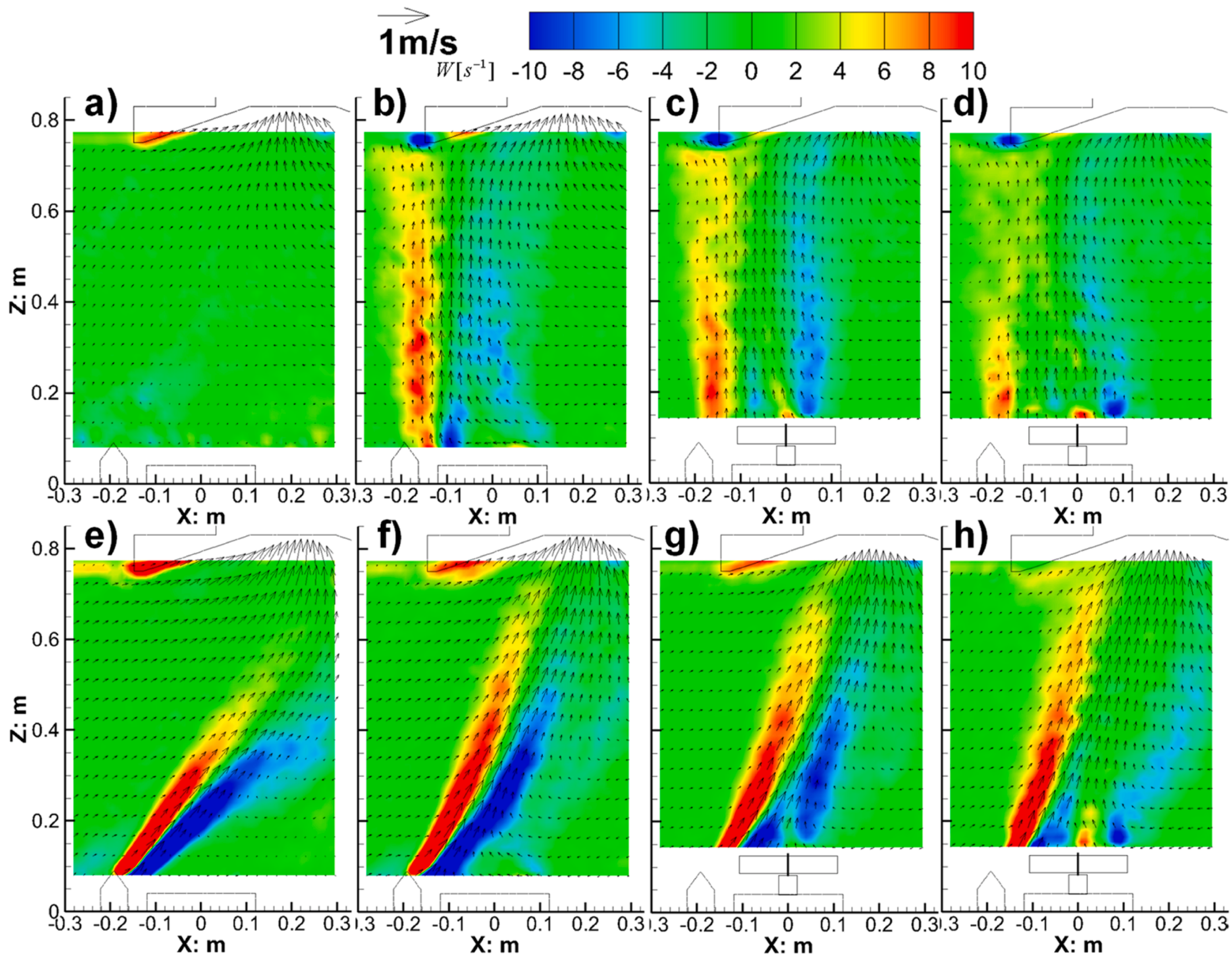

Fig. 9. Time-averaged vorticity field of cases: (a) 300 m^3/h - 0 m/s - iso; (b) 300 m^3/h - 0 m/s - heating; (c) 300 m^3/h - 0 m/s - 30 rpm; (d) 300 m^3/h - 0 m/s - 60 rpm; (e) 360 m^3/h - 0.8 m/s - iso; (f) 360 m^3/h - 0.8 m/s - heating; (g) 360 m^3/h - 0.8 m/s - 30 rpm; (h) 360 m^3/h - 0.8 m/s - 60 rpm.

velocity of the capture jet. Moreover, Fig. 10b shows that the extension line of the capture jet centerline can intersect with the center of the exhaust outlet. This result indicates that the captured jet with $V_0 = 0.8$ m/s exhibits relatively good airflow performance.

The capture jet centerline of most cases in Fig. 10 exhibited a clear linear relationship, except for the case at $V_0 = 0.4$ m/s and Q = 300 m^3/h. The dimensionless trajectories of capture jet centerline can be generalized as Eq. (9). The coefficient K_1 is summarized in Table 3.K_1 increases with Q and decreases with V_0, both for isothermal and heating conditions. Table 3 shows that for cases under isothermal conditions, the coefficients of determination (R^2) of the fitted models were all near 0.99, and the root mean square errors (RMSE) ranged from 0.21 to 0.46. For cases under heating conditions, the R^2 values ranged from 0.93 to 0.99, and the RMSE values ranged from 0.82 to 1.43. These results demonstrate that the trajectory of the capture jet centerline velocity can be reliably predicted by the fitting model (Eq. (9)) under both isothermal and heating conditions.

$$Z / h = K_1 X / h \tag{9}$$

Fig. 11 plots the dimensionless jet centerline velocity decay of some cases in Table 2. In most cases, the dimensionless velocity V_0 / V_c shows a linear relationship with dimensionless distance L/h. The centerline velocity decay coefficient $K_2$of the capture jet, determined via linear regression (Fig. 11), can be fitted by Eq. (10) [30].

$$V_0 / V_c = K_2(L / h) + 1 \tag{10}$$

where V_c is the centerline velocity of the capture jet at distance L.

Table 3 also summarizes the values of K_2. As shown in Table 3, K_2 of cases under isothermal conditions decreases with the increase of V_0. While, K_2 of cases under heating conditions increases with V_0.K_2 of cases with $V_0 = 0.8$ m/s increases with Q, both under isothermal and heating conditions. Table 3 also indicates that the K_2 of the capture jet under heating conditions is smaller than the corresponding cases under isothermal conditions. It might be due to the jet entraining more air under heating conditions, resulting in a lower K_2. Fig. 11b compares K_2 for the cases with and without disturbance at V_0 = 0.8 m/s. Fig. 11b demonstrates that even with the disturbance, the jet centerline velocity decay can still be fit by Eq. (8). As shown in Fig. 11b and Table 3, although the trajectories of the capture jet centerline are almost overlapping (see Fig. 10b), the high disturbance speed results in a higher K_2. Table 3 shows that under isothermal conditions, the R^2 values ranged from 0.96 to 0.99, and the RMSE values ranged from 0.03 to 0.08. Under heating conditions, the R^2 values ranged from 0.89 to 0.97, the RMSE values ranged from 0.02 to 0.06. These results indicate that the fitting model (Eq. (10)) can well predict the jet centerline velocity decay under both isothermal and heating conditions.

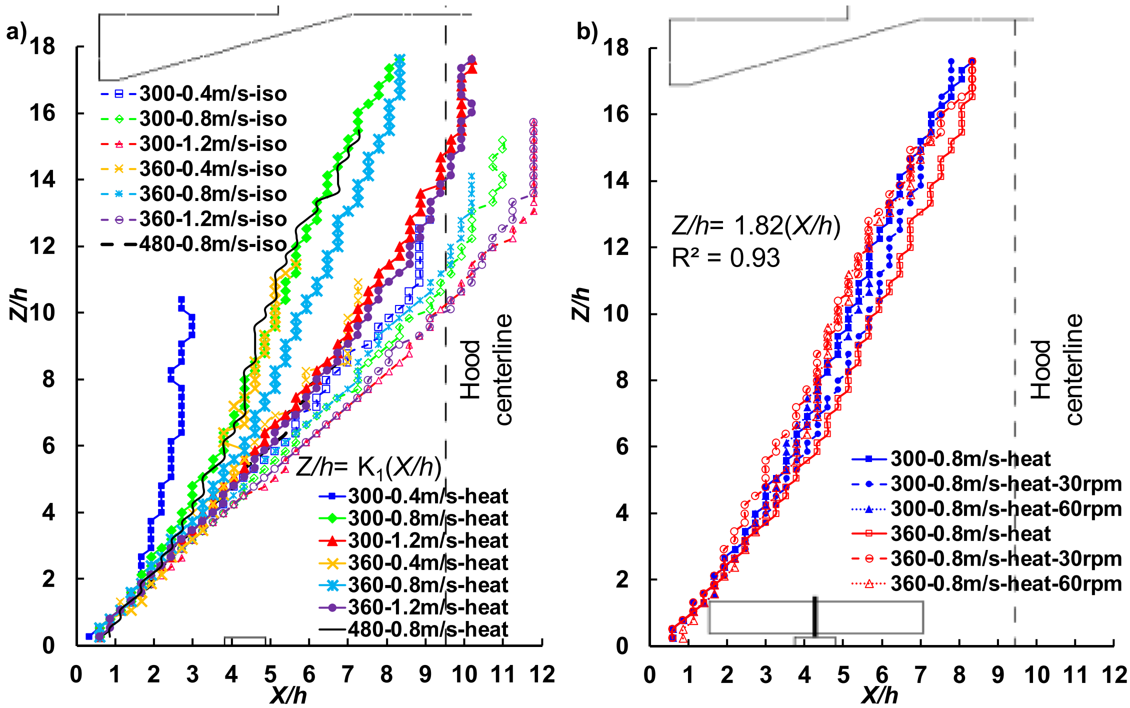

Fig. 10. Dimensionless trajectory of the capture jet centerline velocity at: (a) different velocity of capture jet and exhaust flowrate; (b) different disturbance speed.

Table 3
The K_1 and K_2 values of different cases.

Exhaust Flowrate (m^3/h)	Capture jet Velocity (V_0) (m/s)	Condition	K_1	K_1 - R^2	K_1 - RMSE	K_2	K_2 - R^2	K_2 -RMSE
300	0.4	isothermal	1.20	0.99	0.23	0.125	0.98	0.06
300	0.8	isothermal	1.17	0.99	0.46	0.056	0.98	0.04
300	1.2	isothermal	1.05	0.99	0.21	0.054	0.99	0.04
360	0.4	isothermal	1.31	0.99	0.32	0.096	0.99	0.03
360	0.8	isothermal	1.18	0.99	0.37	0.073	0.99	0.04
360	1.2	isothermal	1.09	0.99	0.35	0.055	0.98	0.04
480	0.8	isothermal	1.18	0.99	0.39	0.092	0.96	0.08
300	0.4	heating	-	-		-	-	-
300	0.8	heating	2.01	0.95	1.12	0.019	0.89	0.04
300	0.8	heating - 30 rpm	1.91	0.93	1.43	0.018	0.93	0.02
300	0.8	heating - 60 rpm	1.78	0.98	0.83	0.035	0.93	0.05
300	1.2	heating	1.48	0.99	1.00	0.041	0.95	0.05
360	0.4	heating	1.65	0.97	1.41	-	-	
360	0.8	heating	1.80	0.94	1.27	0.032	0.93	0.05
360	0.8	heating –30 rpm	2.05	0.99	1.34	0.030	0.94	0.03
360	0.8	heating - 60 rpm	1.95	0.98	0.82	0.091	0.93	0.06
360	1.2	heating	1.44	0.98	1.15	0.043	0.95	0.05
480	0.8	heating	1.95	0.98	1.26	0.071	0.97	0.05

3.4. Particle concentration field

Fig. 12 compares the time-averaged particle concentration (gray-scale, C_g) fields for some cases acquired using a scattering grayscale method with the PIV system. Fig. 12 provides a visual representation of containment effectiveness. The time-averaged particle concentration fields in Fig. 12a and Fig. 12b illustrate containment failure with significant particle escape from the cooking zone for the cases without the capture jet and with a low-speed capture jet, respectively. The escape of particles might be caused by cooking thermal plume perturbations and high concentration differences. As shown in Fig. 12c–e, with the V_0 was increased to 0.8 m/s, the particles were effectively contained within the capture zone and captured by push-pull flow under various disturbance speeds (0, 30, 60 rpm). This phenomenon is consistent with the oil fume visualization experiments conducted on an air-curtain exhaust system [13]. Huang et al. [13] found that a single upward capture jet with $V_0 =$ 1 m/s at the front edge of the stove could mitigate the adverse impact of cross-draft and elevate the CE of the exhaust hood. By comparing the particle concentration fields in Fig. 12c–e, it can be found that the disturbance can weaken the effect of entraining and aggregating particles by the capture jet. Therefore, the radius and area of the particle cluster in the measurement section for cases with disturbance are larger than those without disturbance. It might be because the disturbance causes the flow near the pan from a vortex in the cross-section, thereby expanding the area of the particle cluster. With the V_0 was increased to 1.2 m/s, another circular particle cluster appeared on the upper right side of the capture jet (see Fig. 12f). This may be attributed to the highly pulsating nature of the high-velocity jet, whose containment was compromised by excessive momentum. Besides, the suction flow was destroyed due to the capture jet with a large velocity. The jet flow with large velocity will impinge on the range hood, resulting in an increase in convective escape of particles. In general, the result in Fig. 12 indicates that the captured jet can exhibit relatively good capture performance at $V_0 = 0.8$ m/s.

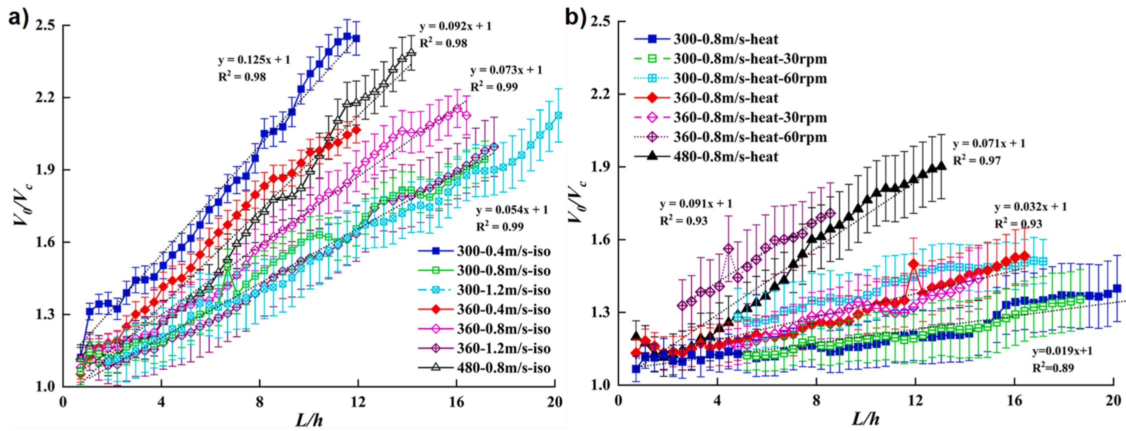

Fig. 11. Dimensionless jet centerline velocity decay at: (a) different velocity of capture jet and exhaust flowrate; (b) different disturbance speed. Error bars represent standard deviation.

The water vapor is also a key factor in real cooking plumes and pollutant dispersion. However, because water vapor would interfere with the measurements of the flow field and the particle concentration field, its generation was intentionally excluded from the experimental setup. This simplification in the present study was made to isolate the effects of ventilation conditions and particle dynamics without the additional complexity of humidity-driven processes. Lv et al. [24,43] and Xie et al. [44] used water vapor visualization experiments to analyze the morphology and evolution of the thermal plume, as well as the effects of different stages of human walking on water vapor flow. Although water vapor visualization makes it difficult to quantify the plume velocity, it can still serve as a visual tracer to reflect the fluctuating characteristics of the thermal plume and pollutant dispersion [24,43, 44]. Future experimental studies will further investigate the effects of cooking oil fumes, water vapor, and their mixtures on pollutant dispersion modeling.

3.5. Particle capture efficiency

Fig. 13 presents the particle CEs of cases with different push-pull airflow rates and disturbance speeds. As shown in Fig. 13, the particles CEs increased with the exhaust flowrate. This result agrees with previous studies [35,39]. Fig. 13 compares the particle CEs for cases with various V_0 of the capture jet and Q at 360 m^3/h, the capture jet exhibits the highest CE at $V_0 = 0.8$ m/s. The total CE for the case with $V_0 = 0.8$ m/s and Q = 360 m^3/h (480 m^3/h) is 95.9% (97.1%). The total CE for the case with Q at 360 m^3/h and 480 m^3/h ($V_0 = 0$ m/s) is 81.8% and 86.6%, respectively. The total CEs for the cases with $V_0 = 0.8$ m/s and Q = 360 m^3/h (or 480 m^3/h) are higher by 14% than those of the corresponding cases without a capture jet. The air flowrate required by the capture jet at $V_0 = 0.8$ is only 22 m^3/h. By comparison, the total CE for the case with Q at 480 m^3/h is only 4.7% higher than that of the case with Q at 360 m^3/h. This result indicates that improving the airflow distribution of the exhaust system to enhance the CE is much more effective than simply increasing the exhaust flowrate. The measurement results from 120 occupied residences conducted by Yin et al. [20] show that the mean effective Q was only 312–516 m^3/h, even with the door fully open. The reasonable capture airflow (see Figs. 6 and 7) and acceptable CE (Fig. 13) with $V_0 = 0.8$ m/s and Q at 300–480 m^3/h indicated that the proposed ventilation system in our study could be used well in real residential kitchens.

Fig. 13 shows that the CE of ultrafine particles (UFP) increases with particle size for all cases. This result is consistent with the experimental study [45] with low exhaust flowrates. The size-resolved particle capture efficiency distributions in Fig. 13 showed a two-valley distribution. The first valley particle is 0.3–0.5 μm in size. The second valley particle is 1.7–2.1 μm in size. The particle range agrees with the experimental study [39] regarding the low particle capture efficiency at 0.3–2 μm. These valley particle sizes can be used as the identification particle size for future simulation and optimization design. The impact of the simulated cooking operation on the CEs increased with the disturbance speed (see Fig. 13). This disturbance could reduce the total CE by up to 5%. The disturbance could reduce the CE of some particle sizes by up to 10%. The extent of the cooking operation on the CE is comparable to the interference caused by HVAC diffusers in the kitchen [22]. The effects of disturbance by long-term [22,23] and short-term [24,25] human walk-by motions on the CE are also not to be ignored. The impacts of these interference factors on the CE of the new exhaust hood proposed in the present study need to be addressed in future studies.

Table 4 compares the pollutant capture performance of this new exhaust hood with that of previous investigations involving air curtains. Compared with most studies [10,11,15,16], the new exhaust system achieves favorable capture performance at lower exhaust and air curtain supply flowrates. This indicates that the new system can effectively reduce exhaust energy consumption. Moreover, given the relatively low effective exhaust flow rate of range hoods in high-rise residential buildings [20], this new system is particularly suitable for application in real residential kitchens. With the exception of Huang et al. [21], the air curtain supply angle was set to 90° in all other studies. The results from Ref. [21] and our study indicate that the airflow pattern with the inclined capture jet directed straight toward the exhaust outlet enables more effective containment of the cooking thermal plume and pollutant dispersion.

4. Conclusion

The flow characteristics and capture performance of a new push-pull exhaust system in a residential kitchen were investigated in this research. The major conclusions are summarized.

(1) This study demonstrates that the proposed push-pull system achieves effective airflow containment by transitioning the flow field from being dominated by chaotic thermal plumes to a forced convection regime controlled by the capture jet. This creates an organized airflow that successfully channels pollutants toward the exhaust. The deflection and decay of the capture jet are influenced by the exhaust flowrate, jet velocity, and thermal conditions. The deflection angle of the capture jet under heating conditions is larger than that under isothermal conditions. The deflection angle increases with the exhaust flowrate, and decreases with the jet velocity. Empirical linear models for jet

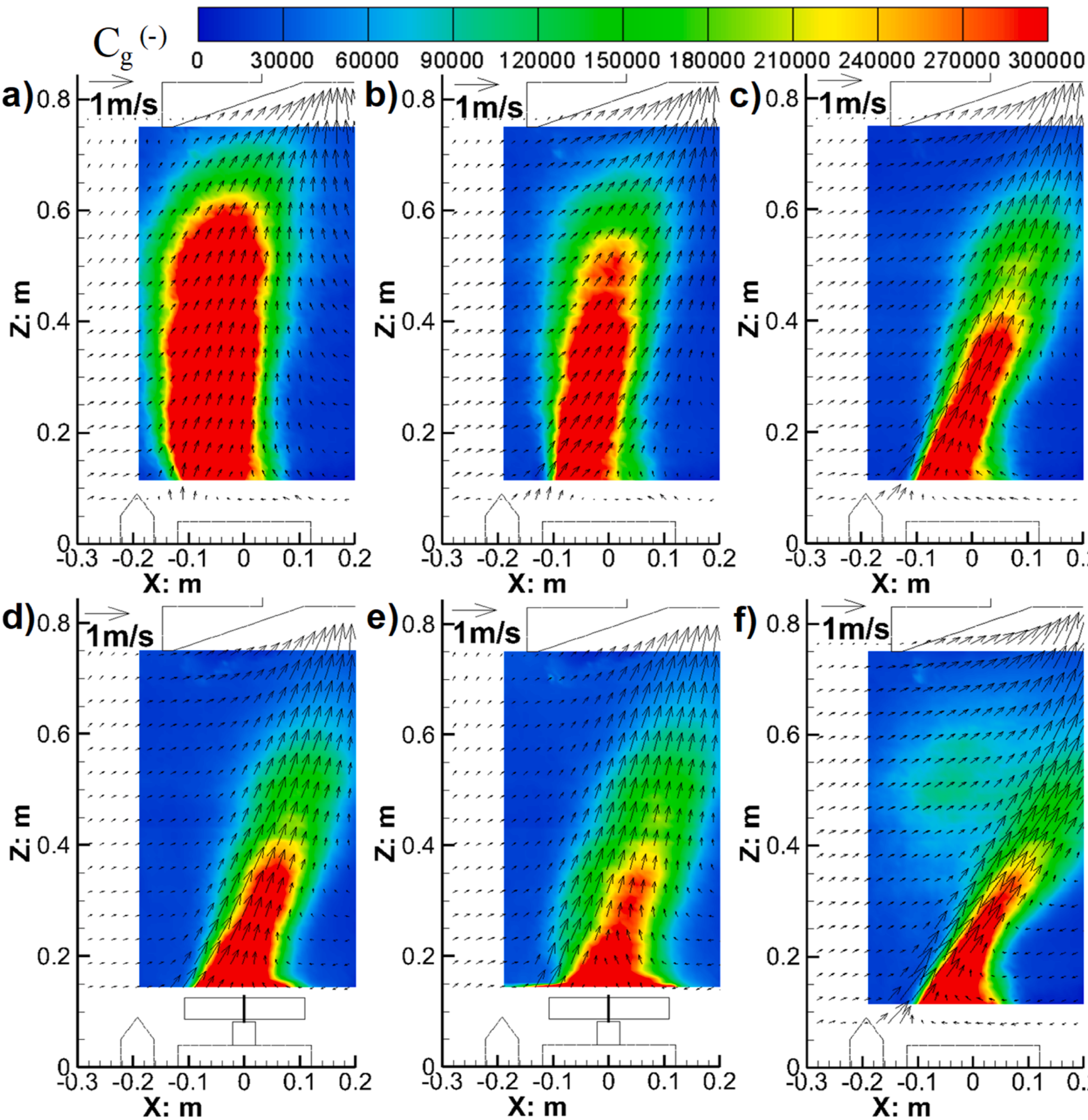

Fig. 12. The time-averaged particle grayscale (C_g) fields: (a) 360 m^3/h - 0 m/s; (b) 360 m^3/h - 0.4 m/s; (c) 360 m^3/h - 0.8 m/s; (d) 360 m^3/h - 0.8 m/s - 30 rpm; (e) 360 m^3/h - 0.8 m/s - 60 rpm; (f) 360 m^3/h - 1.2 m/s.

centerline trajectory and velocity decay can describe these relationships.

(2) Although the simulated cooking operation disturbance increased the entrainment radius of the jet and the area of particle clusters, it had a negligible effect on the deflection angle and trajectory of the jet centerline. With a capture jet velocity of 0.8 m/s, the robustness of the air containment zone against typical cooking motions is demonstrated. The impact of the simulated cooking operation on CE increased with the disturbance speed. The disturbance could reduce the total CE by up to 5% and the CE for specific particle sizes by up to 10%.

(3) The capture jet demonstrates optimal containment and capture performance for the novel exhaust hood with a velocity of 0.8 m/s. The capture jet achieved total particle CEs of up to 95.9%–97.1% at exhaust flowrates of 360–480 m^3/h. The capture jet significantly improves total particle CE by up to 14% compared to corresponding cases without the capture jet.

(4) The study confirmed that the CE of UFP increases with particle size. The size-resolved particle CE of $PM_{0.02–10}$ exhibited a two-valley distribution. The particles in the size ranges of 0.3–0.5 μm and 1.7–2.1 μm have relatively low CE. These valley particle size ranges can represent critical points for future simulation and optimization of ventilation systems. The high-resolution experimental data also provide valuable benchmarks for future computational fluid dynamics simulations and the development

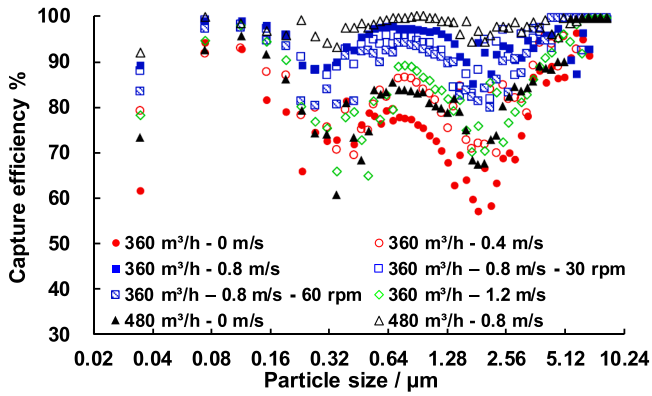

Fig. 13. The $PM_{0.02-10}$ particle capture efficiency of different cases.

Table 4
Comparison of pollutant capture performance across different studies.

Air curtain type	Refs.	Exhaust Flowrate (m^3/h)	Air curtain details	Comment
Downward, three slots	Liu et al., 2014 [10]	630	36 m^3/h, 1.5 m/s, −5°	Leakage rate mitigated by 2 orders vs. baseline.
Downward, one slot	Cao et al., 2017 [11]	504–564	64.8–90.1 m^3/h, 1.8–2.5 m/s, 90°, at the front edge of the range hood.	Intake fraction mitigated by 2–3 orders vs. baseline.
Upward, one slot	Huang et al., 2011 [21]	504–606	41.7 m^3/h, 1 m/s, 75°, at the front edge of the stove.	Leakage rate mitigated by 2 orders vs. baseline.
Upward, three slots	Cao et al., 2017 [11]	504–564	49–73.5 m^3/h, 1–1.5 m/s, 90°, around the cooker.	Intake fraction mitigated by 2 orders vs. baseline.
Upward, four slots	Zhou et al., 2019 [16]	444–519	157 m^3/h, 0.5 m/s, 90°	CE: 91.7%–96%.
Upward, three slots	Liu et al., 2020 [18]	750	450 m^3/h, 1.54 m/s, 90°	CE: 93.1%–98.5%.
Upward, three slots	Liu et al., 2024 [15]	500	136 m^3/h, 1.2 m/s, 90°	CE: 95.2%.
Upward, one slot	Our investigation	360–480	22 m^3/h, 0.8 m/s, 47.5°, at the side edge of the stove.	CE: 95.9%–97.1%.

of adaptive control strategies that are suitable for different cooking conditions.

CRediT authorship contribution statement

Wenhua Chen: Writing – original draft. **Mengyang Yan:** Data curation. **Yunxiang Cui:** Formal analysis. **Yanzhe Yu:** Investigation. **Jing Xu:** Funding acquisition. **Junjie Liu:** Project administration, Methodology. **Jiayu Li:** Supervision.

Declaration of competing interest

The authors declare that they have no known competing financial interests or personal relationships that could have appeared to influence the work reported in this paper.

Acknowledgment

The research was supported by the National Natural Science Foundation of China (No. 52268019), Jiangxi Provincial Natural Science Foundation (20242BAB20221).

Data availability

Data will be made available on request.

References

[1] W. Yang, B. Zhao, Exposure to PM1 and PM2.5 among household cooking members, Build. Environ. 283 (2025) 113430.
[2] X. Xu, K. Hu, Y. Zhang, J. Dong, C. Meng, S. Ma, Z. Liu, Experimental evaluation of the impact of ventilation on cooking-generated fine particulate matter in a Chinese apartment kitchen and adjacent room, Environ. Pollut. 348 (2024) 123821.
[3] Y. Zhao, L. Li, W. Zhang, S. Liu, W. Wang, X. Ji, D. Yang, L. Zhao, Z. Zhang, X. Guo, F. Deng, Associations of indoor airborne microbiome with systemic inflammation in the context of indoor particulate matter pollution and the metabolic mechanisms, J. Environ. Sci. 159 (2026) 187–198.
[4] Y. Deepthi, A. Passi, V.S. Chithra, U. Schlink, S.M.S. Nagendra, Personal exposure of women to PM2.5-bound PAH derivatives from cooking emissions in varied rural kitchen setups, Build. Environ. 267 (2025) 112189.
[5] J. Hu, L. Yang, N. Kang, N. Wang, L. Shen, X. Zhang, S. Liu, H. Li, T. Xue, S. Ma, T. Zhu, Associations between long-term exposure to fine particulate matter and its constituents with lung cancer incidence: evidence from a prospective cohort study in Beijing, China, Environ. Pollut. 368 (2025) 125686.
[6] W. Chen, J. Liu, C.M. Mak, P. Wang, L. Zhao, H.M. Wong, Near fields of annular slotted hoods measured via 2D-PIV, Build. Environ. 144 (2018) 1–8.
[7] S. Liu, J. Dong, Q. Cao, X. Zhou, J. Li, X. Lin, K. Qing, W. Zhang, Q. Chen, Indoor thermal environment and air quality in Chinese-style residential kitchens, Indoor Air 30 (2) (2020) 198–212.
[8] O. Han, A. Li, R. Kosonen, Hood performance and capture efficiency of kitchens: a review, Build. Environ. 161 (2019) 106221.
[9] J. Zhang, J. Gao, J. Wang, C. Cao, M. Xie, L. Zeng, L. Lv, The performance of different ventilation methods in residential kitchens with different spatial organizations: a literature review, Build. Environ. 201 (2021) 107990.
[10] X. Liu, X. Wang, G. Xi, Orthogonal design on range hood with air curtain and its effects on kitchen environment, J. Occup. Environ. 11 (3) (2014) 186–199.
[11] C. Cao, J. Gao, L. Wu, X. Ding, X. Zhang, Ventilation improvement for reducing individual exposure to cooking-generated particles in Chinese residential kitchen, Indoor Built. Environ. 26 (2) (2017) 226–237.
[12] W. Chen, J. Liu, J. Li, X. Dai, P. Wang, C. Wang, Assessment of a confined thermal plume by PIV combined with POD analysis, Appl. Therm. Eng. 188 (2021) 116590.
[13] J.K. Chen, Flow characteristics of an inclined air-curtain range hood in a draft, Ind. Health 53 (4) (2015) 346–353.
[14] J. Li, A. Liu, L. Yu, C. Meng, Y. Ma, J. Dong, Influence and optimal operating parameters of slit make-up air system on low-energy kitchen environment, J. Build. Eng. 94 (2024) 110016.
[15] Y. Liu, C. Li, H. Ma, X. Luo, Performance of local supply-exhaust ventilation around stove with numerical simulation in a residential kitchen, J. Build. Eng. 87 (2024) 109078.
[16] B. Zhou, P. Wei, M. Tan, Y. Xu, L. Ding, X. Mao, Y. Zhao, R. Kosonen, Capture efficiency and thermal comfort in Chinese residential kitchen with push-pull ventilation system in winter-a field study, Build. Environ. 149 (2019) 182–195.
[17] Y. Song, X. Chen, Z. Zhang, S. Cao, T. Du, H. Guo, Studies on the control of kitchen pollutants by exhaust hood with air-filled slots, J. Build. Eng. 48 (2022) 103891.
[18] S. Liu, Q. Cao, X. Zhao, Z. Lu, Z. Deng, J. Dong, X. Lin, K. Qing, W. Zhang, Q. Chen, Improving indoor air quality and thermal comfort in residential kitchens with a new ventilation system, Build. Environ. 180 (2020) 107016.
[19] R.F. Huang, G.Z. Dai, J.K. Chen, Effects of mannequin and walk-by motion on flow and spillage characteristics of wall-mounted and jet-isolated range hoods, Ann. Occup. Hyg. 54 (6) (2010) 625–639.
[20] Y. Yin, J. Pei, J. Liu, The effectiveness of kitchen ventilation for organic gaseous compound control in Chinese residential buildings, Build. Environ. 226 (2022) 109764.
[21] R.F. Huang, Y.C. Nian, J.K. Chen, K.L. Peng, Improving flow and spillage characteristics of range hoods by using an inclined air-curtain technique, Ann. Occup. Hyg. 55 (2) (2011) 164–179.
[22] T. Kurabuchi, H.S.S. Lee, Feasibility study of CFD prediction for evaluation of commercial kitchen environments, in: Proceedings of the 13th Conference of International Building Performance Simulation Association, 2013, pp. 776–783.
[23] T. Iwamatsu, W. Urabe, Influence of air disturbance caused by cooking behavior on capture efficiency of exhaust hood in Japanese commercial kitchens, ASHRAe Trans. 121 (2015) 1LL.
[24] L. Lv, L. Zeng, Y. Wu, J. Gao, W. Xie, C. Cao, Y. Chen, J. Zhang, Effects of human walking on the capture efficiency of range hood in residential kitchen, Build. Environ. 196 (2021) 107821.
[25] L. Lv, Y. Wu, C. Cao, L. Zeng, J. Gao, W. Xie, J. Zhang, Impact of different human walking patterns on flow and contaminant dispersion in residential kitchens: dynamic simulation study, Build. Simul. 15 (6) (2022) 1051–1066. China.

[26] W. Chen, J. Li, C. Wang, X. Dai, J. Liu, 2D-PIV measurement of range hood-driven flow in a domestic kitchen, Energy Build. 177 (2018) 64–76.
[27] W. Li, T. Hasama, A. Chong, J.G. Hang, B. Lasternas, K.P. Lam, K.W. Tham, Transient transmission of droplets and aerosols in a ventilation system with ceiling fans, Build. Environ. 230 (2023) 109988.
[28] L. Zhao, R. You, J. Liu, Q. Chen, A real-time measurement and analysis method for gas holdup in a wet scrubber with the use of image information entropy, Sep. Purif. Technol. 345 (2024) 127255.
[29] A. Sankaran, R. Hain, C.J. Kähler, Particle image based simultaneous velocity and particle concentration measurement, Meas. Sci. Technol. 35 (6) (2024) 065206.
[30] A. Li, C. Yang, T. Ren, X. Bao, E. Qin, R. Gao, PIV experiment and evaluation of air flow performance of swirl diffuser mounted on the floor, Energy Build. 156 (2017) 58–69.
[31] GB/T 17713-2011 Range Hood, General Administration of Quality Supervision, Inspection and Quarantine of the People's Republic of China, 2011.
[32] M. Sandberg, Whole-field measuring methods in ventilated rooms, HVAC&R Res. 13 (6) (2007) 951–970.
[33] X. Cao, J. Li, J. Liu, W. Yang, 2D-PIV measurement of isothermal air jets from a multi-slot diffuser in aircraft cabin environment, Build. Environ. 99 (2016) 44–58.
[34] J. Gao, C. Cao, X. Zhang, Z. Luo, Volume-based size distribution of accumulation and coarse particles (PM0.1–10) from cooking fume during oil heating, Build. Environ. 59 (2013) 575–580.
[35] Y.S. Kim, I.S. Walker, W.W. Delp, Development of a standard capture efficiency test method for residential kitchen ventilation, Sci. Technol. Built. Environ. 24 (2) (2018) 176–187.
[36] C. Chen, Y. Zhao, B. Zhao, Emission rates of multiple air pollutants generated from Chinese residential cooking, Environ. Sci. Technol. 52 (3) (2018) 1081–1087.
[37] J. Gao, C. Cao, Q. Xiao, B. Xu, X. Zhou, X. Zhang, Determination of dynamic intake fraction of cooking-generated particles in the kitchen, Build. Environ. 65 (2013) 146–153.
[38] J. Gao, C. Cao, L. Wang, T. Song, X. Zhou, J. Yang, X. Zhang, Determination of size-dependent source emission rate of cooking-generated aerosol particles at the oil-heating stage in an experimental kitchen, Aerosol. Air. Qual. Res. 13 (2) (2013) 488–496.
[39] M.M. Lunden, W.W. Delp, B.C. Singer, Capture efficiency of cooking-related fine and ultrafine particles by residential exhaust hoods, Indoor Air 25 (1) (2015) 45–58.
[40] L.L. Yeung, W.M. To, Size distributions of the aerosols emitted from commercial cooking processes, Indoor Built. Environ. 17 (3) (2008) 220–229.
[41] S.W. See, R. Balasubramanian, Risk assessment of exposure to indoor aerosols associated with Chinese cooking, Environ. Res. 102 (2) (2006) 197–204.
[42] M.V. Pham, F. Plourde, S.D. Kim, Effect of swirl on pure turbulent thermal plume development, Int. J. Heat Fluid Flow 27 (3) (2006) 502–513.
[43] L. Lv, J. Gao, L. Zeng, C. Cao, J. Zhang, L. He, Performance assessment of air curtain range hood using contaminant removal efficiency: an experimental and numerical study, Build. Environ. 188 (2021) 107456.
[44] W. Xie, J. Gao, L. Lv, C. Cao, Y. Hou, X. Wei, L. Zeng, Exhaust rate for range hood at cooking temperature near the smoke point of edible oil in residential kitchen, J. Build. Eng. 45 (2022) 103545.
[45] D. Rim, L. Wallace, S. Nabinger, A. Persily, Reduction of exposure to ultrafine particles by kitchen exhaust hoods: the effects of exhaust flow rates, particle size, and burner position, Sci. Total Environ. 432 (2012) 350–356.